High frame rate color Doppler echocardiography: a quantitative comparison of different approaches

High frame rate color Doppler echocardiography: a quantitative comparison of different approaches

Alessandro Ramalli, Alfonso Rodriguez-Molares, Jørgen Avdal, Jan D'hooge, and Lasse Løvstakken

Abstract—Ultrasound color Doppler imaging (CDI) provides a map of the axial blood flow velocities in a 2D/3D region of interest. While CDI is clinically effective for a qualitative analysis of abnormal blood flows, e.g. for valvular disease in cardiology, it is in limited use for quantitative measures, mainly hampered by low frame rate and measurement bias. These limitations can be reduced by different approaches towards high frame rate (HFR) imaging at the expense of reduced image quality and penetration depth. The aim of this study was to quantitatively compare the impact of different HFR sequences on CDI. Different cardiac scan sequences, including diverging waves and multi-line transmission, were designed, implemented on a research system, and compared in terms of patient safety parameters, image quality, and penetration depth. Further, in-vivo images were acquired and compared for healthy volunteers. Results showed that HFR techniques spread artifacts on larger areas compared to standard single line scans (> +50%). Also, due to patient safety limitations, they reduce the penetration depth up to −5 cm. On the other hand, HFR techniques provide comparable velocity estimates (relative difference < 6%) and enhance the time resolution of color Doppler images, achieving frame rates up to 625 Hz in continuous acquisition.

Index Terms—Cardiac imaging, echocardiography, high frame rate, color Doppler, color flow, multiline transmission, diverging waves, clinical.

I. INTRODUCTION

The annual reports of the heart associations show that cardiovascular diseases (CVDs) still remain a major cause of mortality and morbidity in the Western developed countries [1], [2]. Since major CVDs are associated with dysfunction of the left ventricle (LV) [3], its accurate functional assessment is essential.

Ultrasound color Doppler imaging (CDI) provides 2D real-time images for a global and qualitative view of the average axial blood flow [4], [5], [6, Ch. 11]. In cardiac applications, it is most useful for the assessment of valve stenosis, valve regurgitation [7], [8], and intracardiac shunts, i.e. the presence of flow across an atrial or ventricular septal defect [9]–[11]. Even if CDI is effective for a qualitative analysis of abnormal blood flows, it is not yet considered useful for quantitative measurements, such as the assessment of ejection fraction, ventricular filling and systolic pressures, and ventricular diastolic function [12]. Indeed, quantitative analysis is still hampered by a compromise between frame rate, field of view, and measurement quality. High frame rate (HFR) imaging techniques [13]–[15] are now being introduced in echocardiography; they could overcome these limitations, but at the cost of reduced image quality (contrast and spatial resolution), which, in turn, might affect the quality of the flow estimates. Moreover, given that HFR scan sequences are typically based on the transmission of defocused waves [16]–[21] or multiple simultaneously focused beams [22]–[26], penetration depth may also become an issue, when considering patient safety limits on acoustic output [27], [28].

The aim of this work was to develop and quantitatively compare the effects of different HFR scan sequences in cardiac CDI also considering patient safety limitations for clinical applicability. For this purpose, different scan sequences were designed, including diverging waves and multi-line transmissions for HFR, as well as single-line transmission as a gold-standard benchmark. The imaging sequences were implemented on the Vantage 256 system (Verasonics, Kirkland, WA, USA), which was connected to a cardiac phased array (P4-2v, Verasonics, Kirkland, WA, USA). Then, sequences were compared in terms of both patient safety related parameters and quality of color Doppler images, when scanning a 90° wide, 12cm deep sector. Finally, preliminary in-vivo recordings were acquired from healthy volunteers.

The paper is organized as follows: Section II introduces the characteristic parameters of focused and unfocused waves, recalls the basics of color flow imaging, details the experimental and in-vivo setups, and defines the comparison metrics; Section III shows experimental results and in-vivo images; Section IV provides the discussion and concludes with possible perspectives.

II. METHODS

A. High frame rate imaging modes

The frame rate achieved in B-mode imaging is defined as:

$$FR = \frac{PRF}{nTX} \tag{1}$$

where PRF is the pulse repetition frequency and nTX is the number of transmission events required to reconstruct a full B-mode frame. In phased array imaging, nTX is linked to the sector angle (2θ), the number of lines per frame ($nLines$), and the number of lines beamformed in parallel for each transmission. However, in CDI, the transmission along a given direction θ_{TX} should be repeated N_P times (also called packet size) to achieve a reasonable clutter rejection and a good signal-to-noise ratio on the final images. Hence, the final CDI frame rate is

$$FR_{CDI} = \frac{FR}{N_P} = \frac{PRF}{nTX \cdot N_P} \tag{2}$$

In this paper, images were reconstructed by scanning the region of interest (ROI) with both (multiple) focused [23], [24] and diverging waves [18], [19], [29]. On reception, parallel beamforming was implemented using synthetic transmit beams (STB) [30], [31]. This technique requires a partial overlap between neighboring beams in transmission and allows limiting the artifacts in the transition regions, where the misalignment between beams in transmission and reconstructed lines is more prominent.

1) Focused scan sequences

For focused imaging, both single (SLT) and multi-line transmission (MLT) schemes were used. Fig. 1-top defines the related transmission and reception parameters.

In multi-line transmission imaging, HFR is achieved by simultaneously transmitting $nMLT$ focused beams into different directions ($nMLT$=1 in SLT) and reconstructing, for each beam, $nMLA$ image lines. Hence, the required number of transmission events, to scan the whole region of interest, is

$$nTX = \frac{nLines}{nMLT \cdot nMLA} \tag{3}$$

In order to simultaneously transmit beams with different steering angles θ_{TX}, non-identical electric pulses must be applied to the elements of the phased array transducer. The excitation waveform for a given element is given by the sum of the pulses, each properly delayed, that would be used on that specific element to generate conventional focused SLT beams along the directions of the different MLT lines:

$$\theta_{TX}(i,j) = -\frac{2\theta}{2} + \frac{(nMLA - 1)}{2} \cdot \theta_L + (i - 1) \cdot \theta_B + (j - 1) \cdot \theta_S \tag{4}$$

where $i \in [1, nMLT]$ is the index of the simultaneous MLT beams and $j \in [1, nTX]$ is the index of the transmission event. The step-angle between image lines θ_L, the step-angle between simultaneously transmitted beams θ_B, and the step-angles between consecutive transmission θ_S were defined as:

$$\theta_L = \frac{2\theta}{nLines - 1} \tag{5}$$

$$\theta_B = nTX \cdot nMLA \cdot \theta_L \tag{6}$$

$$\theta_S = nMLA \cdot \theta_L \tag{7}$$

Similarly, the directions of the reconstructed lines were defined as:

$$\theta_{RX}(i,j,k) = \theta_{TX}(i,j) + \left(k - 1 - pOL \cdot nMLA - \frac{(nMLA - 1)}{2} \right) \theta_L \tag{8}$$

where pOL is the amount of overlap between beams in transmission, and $k \in [1, nMLA(1 + 2 \cdot pOL)]$ is the integer index of the overlapping MLA lines.

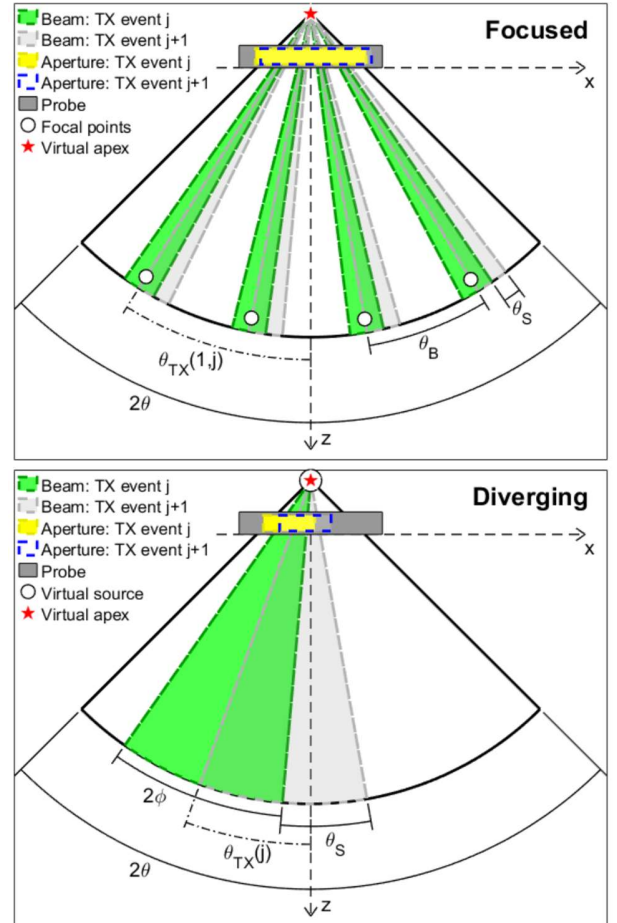The z-coordinate of the virtual apex of the image (z_A) was defined as:

Fig. 1 The reference system and the transmission parameters for the high frame rate scan sequences.

$$z_A = \frac{W_S - W_A}{2 \cdot \tan\left(\frac{2\theta}{2}\right)} \qquad (9)$$

with W_A the width of the full aperture of the probe and W_S the effective width of the subaperture in transmission. By doing so, the subaperture spanned the whole surface of the probe available during the scan, thereby maximizing the width of the region of interest and distributing heat over the whole surface of the probe, so as to avoid overheating only a small portion of the aperture.

2) Diverging scan sequences

Fig. 1 bottom defines the transmission and reception parameters of the diverging wave scan sequences.

Again, the first parameter to be defined is the desired frame rate and hence the number of transmission events per frame. The definition of nTX, together with pOL, determines the aperture angle of the diverging waves as:

$$2\phi = \frac{2\theta}{1 + pOL \cdot (nTX - 1)} \qquad (10)$$

Then, the transmission direction of consecutive beams was computed as

$$\theta_{TX}(j) = -\frac{2\theta}{2} + \frac{2\phi}{2} + (j - 1) \cdot \theta_S \qquad (11)$$

where the step-angle between consecutive transmissions was

$$\theta_S = \lfloor 2\phi \cdot pOL \rfloor_{\theta_L} \qquad (12)$$

Where the operator $\lfloor x \rfloor_{\theta_L}$ denotes the greatest multiple of θ_L greater than or equal to x. Finally, the z-coordinate of the virtual apex z_A corresponded to the position of the virtual sources of the steered diverging waves and was computed as:

$$z_A = -\frac{W_A - p}{2 \cdot \tan\left(\frac{2\theta}{2}\right)} \qquad (13)$$

where p is the element pitch. By doing so, as for focused scan sequences, the subaperture spanned the whole available surface of the probe during the scan.

In order to ensure the same opening angle for all the transmitted diverging waves, a different active subaperture was defined for each transmission event. Specifically, it was defined as the elements included in the range:

$$-z_A \cdot \tan\left(\theta_{TX}(j) - \frac{2\phi}{2}\right) < x$$
$$< -z_A \cdot \tan\left(\theta_{TX}(j) + \frac{2\phi}{2}\right) \qquad (14)$$

Thus, the resulting subaperture size was:

$$W_S(j) = -z_A \cdot \left[\tan\left(\theta_{TX}(j) + \frac{2\phi}{2}\right) - \tan\left(\theta_{TX}(j) - \frac{2\phi}{2}\right) \right] \qquad (15)$$

Finally, the directions of the reconstructed lines were defined as:

$$\theta_{RX}(j,k) = \theta_{TX}(j) - \frac{2\phi}{2} + (k - 1)\theta_L \qquad (16)$$

Where the angle between consecutive image lines θ_L was defined as in (5) and $k \in [1, 2\phi/\theta_L]$.

B. Color Doppler Imaging

In order to extract the blood component of the signals, the clutter was filtered and attenuated by a high-pass polynomial regression filter [32], [33] applied along the slow-time direction. Hence, the velocity of red blood cells was computed by the Kasai estimator [34] that calculates the integral of the phase changes to produce the (lag-one) autocorrelation function, as:

$$R_{N_P}(m) = \frac{1}{N_P - m} \sum_{n=1}^{N_P - m} s(n + m) \cdot s(n)^* \qquad (17)$$

where s is the analytic signal after clutter filtering, * is the complex conjugate, n is the index of consecutive transmissions within the packet, and $m = 1$ is the autocorrelation lag.

Next, incoherent synthetic transmit beams (STB) were computed as suggested in [31]: first, one autocorrelation estimate was calculated from each packet; then, the synthetic autocorrelation estimate $\tilde{R}_{N_P}(m)$ was found by interpolating between the estimates originating from the same position, but from different transmission events, i.e. the overlap region of different beams in transmission. Please, refer to [31] for additional details.

Finally, the flow speed was computed as:

$$v = \frac{c \cdot PRF}{4\pi f_0} \arg\left(\tilde{R}_{N_P}(1)\right) \qquad (18)$$

where c is the speed of sound, f_0 is the central frequency of the received signal (hereinafter considered equal to the central frequency in transmission) and the function $\arg(\cdot)$ computes the phase of the complex argument.

C. Experiments

1) Scan sequences

The color Doppler images obtained with 6 different scan sequences were compared. For all of them, the basic transmitted signal was a 5-cycle, 3 MHz sine burst, tapered with a Hamming window, having a 35% bandwidth at −6dB. The sector angle was 2θ=90° and the number of reconstructed lines was $nLines$=128, thus resulting in a interline step θ_L=0.71°. Moreover, the overlap between beams in transmission was pOL=50%.

Three focused and three diverging scan sequences were considered, as summarized in TABLE I:

SLT-2MLA – This scan sequence was implemented as the gold standard scan sequence. The settings were defined according to conventional (currently available) field of view CDI in order to maximize the signal to noise ratio and

TABLE I
EXPERIMENTAL MODES SETTINGS

Mode name	nLines	2θ	θ_L	pOL	nTX	2ϕ	nMLT	nMLA	W_S [mm]	θ_S	θ_B	z_A [mm]	A [V]
SLT-2MLA	128	90°	0.71°	50%	64	-	1	2	19.2	1.42°	-	0.00	22
SLT-4MLA					32	-	1	4	7.2	2.83°		−6.00	35
4MLT					8	-	4	4	7.2	2.83°	22.7°	−6.00	31
DW20					8	20.6°			[3.5;5.2]	9.92°	-	−9.45	45
DW36					4	36.1°	-	-	[6.3;8.0]	18.0°			35
DW90					1	90.0°			18.9	-			22

penetration depth. Hence, a focused SLT sequence was implemented with 2 lines reconstructed in parallel for each transmitted beam ($nMLA$=2). The whole aperture of the probe was always active, and the focal depth was set to 12 cm, i.e. the maximum depth of interest considered in this work. With the above-mentioned settings the virtual apex position was on the probe surface (z_A=0 mm) and the required number of transmission events was nTX=64.

SLT-4MLA – This scan sequence was also based on SLT, but it was implemented to double the frame rate with respect to the reference mode. Therefore, the same settings as for SLT-2MLA were used, but $nMLA$ was equal to 4, yelding nTX=32. However, according to (8), $nMLA$=4 and pOL=50% require to beamform 8 lines for each transmitted beam. Hence, to ensure a wide enough beam, the active aperture was reduced to W_S=7.2 mm. Such sub-aperture size was determined by Field II simulations [35] to provide, at a depth of 12 cm, a −6dB beam width of $8\theta_L$=5.68°. The small active aperture size allowed moving the virtual apex position to z_A=−6.00 mm.

4MLT – This scan sequence was based on the settings of SLT-4MLA, but $nMLT$ was set equal to 4. Indeed, this was previously shown to be a good tradeoff between image quality, frame rate and signal-to-noise ratio [36]. In this case, nTX was equal to 8, thus resulting in a frame rate 8 times that of the reference mode. It is worth highlighting that the sub-aperture size used for each beam was W_S=7.2 mm, but the global active aperture resulted bigger due to the superposition of 4 beams. Also, partially overlapped pulses, due to the simultaneous transmission of multiple focused beams, would have required 1.7 higher amplitudes than SLT. Hence, amplitudes were normalized to compensate for this effect.

DW20 – This scan sequence was based on diverging wave transmissions; it was defined in order to achieve the same frame rate as the 4MLT sequence. Hence, according to (10), by setting nTX=8, the diverging wave aperture angle was 2ϕ=20.6°. Both the virtual source and the virtual apex position was z_A=−9.45 mm. The position of the virtual source was unchanged between all the scan sequences based on diverging waves since it was determined by the aperture of the probe W_A and the imaging sector angle 2θ, as defined in (13). In this case the sub-aperture size ranged from 3.5 to 5.2 mm depending on the steering direction θ_{TX}, as defined in (15).

DW36 – This scan sequence was based on diverging wave transmissions; it was defined to double the frame rate achieved with DW20 and 4MLT. Again, according to (10), by setting nTX=4, the diverging wave aperture angle was 2ϕ=36.1°. In

this case the sub-aperture size ranged from 6.3 to 8.0 mm.

DW90 – This scan sequence was based on diverging wave transmissions; it was defined to achieve the maximum frame rate, thus reconstructing a whole frame for each transmission event. Hence, by setting nTX=1, the diverging wave aperture angle was 2ϕ=2θ=90.0°. In this case, the achieved frame rate was 64 times higher than the reference mode SLT-2MLA.

It is worth highlighting that no scan sequence was specifically developed for B-mode imaging; hereinafter, B-mode images, when shown, were reconstructed from the same scan sequences used for color Doppler.

2) The Vantage 256 scanner

The experiments were conducted on a Vantage 256 research scanner (Verasonics, Kirkland, WA, USA), providing 256 independent channels both in transmission and reception. Moreover, the Vantage system uses tri-level pulsers where waveforms in transmission can be synthesized at 250 MHz (i.e. on a 4 ns grid). However, as mentioned above, the waveforms needed for MLT are made up of sums of SLT pulses and, to be properly synthesized, they require arbitrary waveform generators (AWGs) and linear transmitters. Hence, in this work, apodization, burst tapering, and waveforms were carefully synthesized using duty-cycle modulation as proposed in [37]. The system was connected to a P4-2v adult cardiac phased array probe (Verasonics, Kirkland, WA, USA); it consisted of 64 elements with a pitch of 300 μm and a 66% bandwidth centered at 3 MHz.

For safety measurements, the system was setup to transmit only the scan sequence under investigation; while, for color Doppler imaging, the system was set to consecutively acquire raw data for 6.0 s, i.e. 1.0 s for each of the 6 scan sequences. Raw channel data were acquired at a sampling rate of 12 MHz and beamformed, through a linearly interpolated delay-and-sum algorithm, in post-processing. The PRF was always set to 5 kHz and the packet size N_P to 8.

3) Normalization of output power

In order to conduct a fair comparison among the performance of the different transmission sequences, the average transmitted power must be considered and equalized. It was computed as:

$$P_T = \frac{A^2 \cdot PRF}{nTX} \cdot \sum_{j=1}^{nTX} \sum_{e=1}^{nEle} \sum_{t} \left(s_{e,j}(t) * h(t) \right)^2 \qquad (19)$$

where $s_{e,j}(t)$ is the tri-level pulser state [−1, 0, 1] at the j-th

transmission event for the e-th element among the $nEle$ active ones, A is the signal amplitude in Volts, and t is the time. $h(t)$ is the impulse response of the transducers, assumed equal for all the elements of the array. P_T was equalized by determining, according to (19), the values of A that ensure the same P_T for all scan sequences. Specifically, in our settings they resulted in 22, 35, 31, 45, 35, 22 V for SLT-2MLA, SLT-4MLA, 4MLT, DW20, DW36, DW90, respectively, as shown in the rightmost column of TABLE I.

It is worth highlighting that including $h(t)$ in (19) is important since only the frequency components of the signals that are within the band limits contribute to the surface heating, while the other components are mainly reflected back to the system front-end. $h(t)$ is especially important when the signals are synthesized with duty-cycle modulated square waves that generate higher order harmonic components.

D. Comparison metrics

The scan sequences were compared in terms of both patient acoustic safety related parameters and CDI quality metrics. The former ones included protection against excessive temperatures and ultrasound radiation.

1) Heating of the probe surface

According to [27], the temperature of the probe was measured during the so-called simulated use. The test consists in measuring the temperature of the probe surface, acoustically coupled to a specifically designed test object to simulate the operating condition. The temperature was measured by a K-type thermocouple (Omega Engineering, Norwalk, CT, USA) in contact with the probe surface through a thermally conductive paste. The test object was a commercial surface temperature test phantom (NPL Management Ltd, Teddington, UK) that respected the specifications defined in [27].

The ultrasound scanner was set to transmit only the scan sequence under investigation while the temperature was monitored with a sampling interval of 1 s. According to [27], to avoid overheating in applications intended for external use, the temperature rise after 30 minutes of continuous transmission should not exceed 10°C.

2) Ultrasound exposure parameters

The thermal index (TI), mechanical index (MI), attenuated spatial-peak temporal-average intensity (I_{spta}), attenuated temporal-average intensity (I_{ta}), and radiated fields were acquired according to the standards and conformity assessment of the International Electrotechnical Commission (IEC) [27], [28]. In particular, the setup included a membrane hydrophone (model HMB-0200, Onda Corporation, Sunnyvale, USA) which was immersed in a tank filled with degassed water. The hydrophone output preamplifier was connected to a digital oscilloscope (PicoScope 5244, Pico Technology, Cambridgeshire, UK), which was in turn connected to a PC. The ultrasound probe, immersed in the water tank, was moved by an automatic positioning system (AIMS III, Onda Corporation, Sunnyvale, USA) capable to adjust 3 orthogonal axes and 3 orthogonal angles.

3) Color Doppler quality metrics

The experimental evaluation of the quality of color Doppler images was based on a commercial Doppler flow simulator (Model 069, CIRS Inc., Norfolk, USA). It consists of a tissue-mimicking material (speed of sound=1540 m/s and attenuation=0.7dB/cm/MHz), which includes an ultrasound-compatible tube. Moreover, it includes a peristaltic pump capable of providing flow rates between 0.5 and 12.5 ml/s.

The scanner was setup as detailed in section (II.C.2) and color Doppler images were computed as detailed in section (II.B). Two regions were defined:
• F_{ROI}: a manually selected region surrounding the tube position, i.e. the region where the blood mimicking fluid flows;
• A_{ROI}: the artifacts region, i.e. an area not including the tube where Doppler signal is shown and can be ascribed to imaging artifacts.

Specifically, A_{ROI} was automatically segmented as the region where the inverse of the coefficient of variation

$$ICV(x,z) = \left| \frac{\mu(x,z)}{\sigma(x,z)} \right| \qquad (20)$$

was greater than a −20dB threshold (arbitrary selected). Here, $\mu(x,z)$ and $\sigma(x,z)$ were the average and standard deviation of the velocity estimates, computed at the specific position (x,z) and along consecutive color Doppler frames. Specifically, high $ICV(x,z)$ values are expected for those points where the color Doppler information is stable between different frames, i.e. for artifacts and flow, while lower values are expected for those points mainly affected by noise. Points already belonging to F_{ROI} were excluded from A_{ROI}.

Considering the two above-mentioned regions, two quality metrics were defined:
• the average relative error (e_r) between velocity estimates $v(x,z)$ obtained with the scan mode under investigation and those obtained with the reference scan mode $v_{SLT-2MLA}(x,z)$; e_r was defined as follows:

$$e_r = \overline{\left| \frac{v(x,z) - v_{SLT-2MLA}(x,z)}{v_{SLT-2MLA}(x,z)} \right|}, \quad (x,z) \in F_{ROI} \qquad (21)$$

• the size of the artifacts area defined as:

$$A_A = \iint\limits_{(x,z)\in A_{ROI}} dx\,dz \qquad (22)$$

E. In-vivo acquisitions

Preliminary in-vivo acquisitions were performed on two healthy volunteers. The scanner was set as detailed in section (II.C.2) and color Doppler images were computed as detailed in section (II.B). The volunteers were scanned in the left lateral decubitus position and acquisitions were performed along different standard views, e.g. apical 3-chamber, 4-chamber, and 2-chamber views.
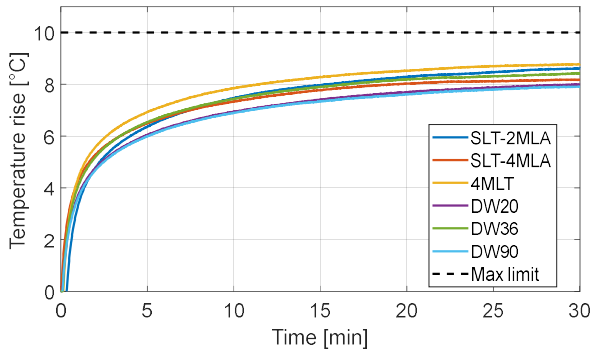
Fig. 2 Temperature rise of the probe surface during simulated test.

Fig. 4 Attenuated temporal-average intensity (I_ta).

III. RESULTS

A. Acoustic output and patient safety related parameters

Fig. 2 shows the results of the measurement for the protection against excessive surface temperatures, conducted according to [27]. Specifically, it shows the temperature rise of the probe surface during the so-called simulated use. For all the scan modes, the temperature rise followed an approximately logarithmic trend and the temperature rise after 30 minutes was at least 1 °C below the limit. Specifically, as shown in TABLE II, the maximum temperature rise (ΔT), for the different scan sequences, remained in the range [7.9, 8.8] °C.

Fig. 3 shows the radiated one-way fields for the different scan sequences, acquired experimentally for safety assessment. They show how the acoustic intensity is spread over the region of interest and how it drops along the main axis of the beam.

Fig. 4 compares the attenuated temporal-average intensity (I_{ta}) along the depth axis for all the scan sequences. An attenuation coefficient of 0.3dB/cm/MHz was considered to provide a conservative safety margin as suggested in [28]. Those curves give an idea on how the signal intensity drops with depth. Specifically, in the range up to 7/8 cm, all the
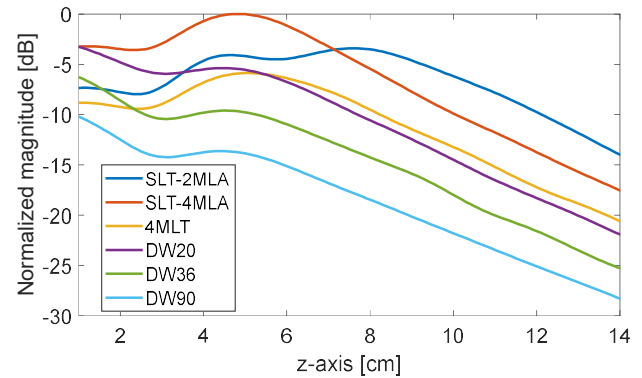
sequences present a local maximum near 5 cm, i.e. the position of the elevation focus due to the acoustic lens of the probe. SLT-2MLA clearly presents a second local maximum due to the electronic focusing, which is not at the expected depth (12 cm) due to attenuation and to the big F-number in transmission of about 6.25. For SLT-4MLA and 4MLT, due to a narrow effective subaperture, the F-number was even larger 16.7, hence the electronic focusing did not have any effect except for limiting the divergence of the beam, as also shown in Fig. 3. Concerning DW transmissions, the trend was similar, while the maximum intensity depended on the aperture angle of the diverging waves: the wider the aperture the lower the field intensity. Specifically, this was a consequence of the limits imposed on the transmitted output energy. On the other hand, for depths higher than 8 cm, the intensity dropped with a rate of about 1.8dB/cm for all the transmission strategies. It is worth nothing that at the last depths of interest (9-14 cm) the average ratios between SLT-2MLA and the other modes are −3.7, −7.1, −8.2, −11.6, −15.1dB for SLT-4MLA, 4MLT, DW20, DW36, DW90, respectively.

TABLE II also reports the MI, TIS, and I_{spta} values for the different modes. It shows that the MI was always well-below the 1.9 limit set by the United States Food and Drug
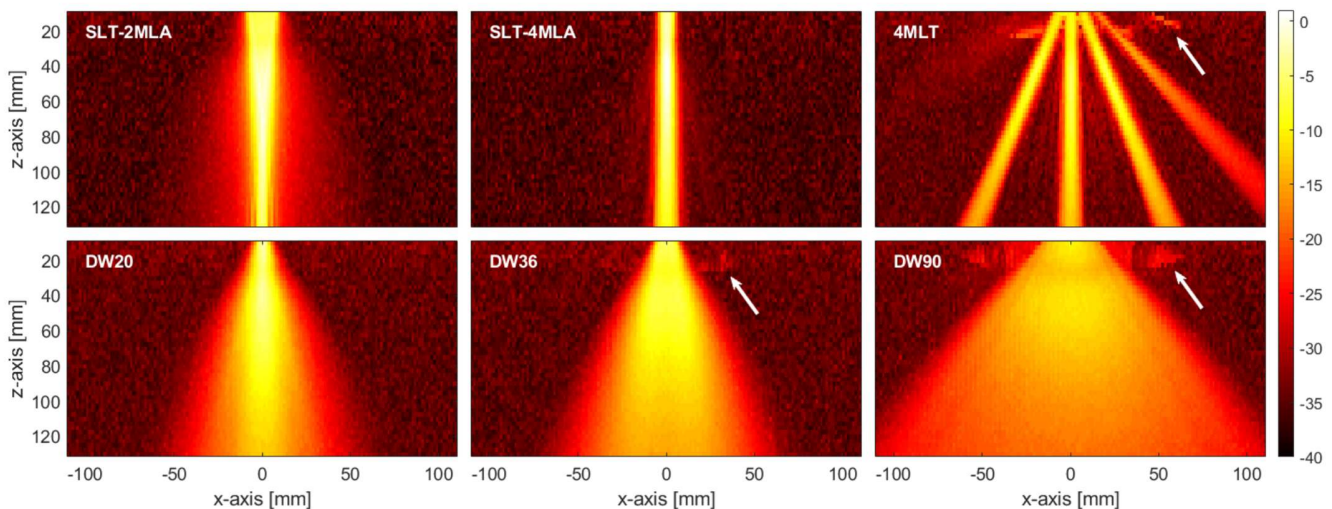
Fig. 3 Measured one-way fields of the negative pressure peak. The colorscale is in dB, normalized with respect to the non-derated peak negative pressure (-1.43 MPa) in SLT-2MLA panel. White arrows point to artifacts due to the long time-window that was set on the oscilloscope; it was needed to record the signals of such wide beams, hence multiple reflections between the membrane hydrophone and the probe surface were also captured at shallower depths.

Administration (FDA). Moreover, it was even lower than the 0.7 limit, below which cavitation is unlikely even if ultrasound contrast agents, containing gas micro-spheres, are used. The FDA also set a limit to 720 mW/cm^2 on the spatial-peak temporal-average intensity (I_{spta}) for all applications (except ophthalmic) that was well-respected for all scan modes, where the maximum value (312.8 mW/cm^2) was achieved with SLT-4MLA. Finally, TIS was in the range [0.6; 1.86] that, according to [38], is safe for examinations with a total ultrasound exposure time (T_{ex} in TABLE II) shorter than 60 minutes.

B. Color Doppler quality metrics

Fig. 5 shows examples of color Doppler images acquired on the flow phantom. Qualitatively they highlight how artifacts spread across CFI frames. On SLT images, artifacts mainly appear deeper than the tube (white arrows), while they also appear at shallower depths for HFR images. In particular, the artifacts are tilted replicas of the tube with 4MLT (cyan arrows) and a wide homogeneous band (green arrows) in DW scan sequences.

Quantitatively, the extension of the area covered by artifacts is reported in TABLE III, where it was normalized by the widest one, i.e. the one of DW90. Specifically, the table shows that the narrower the DW opening angle the smaller the artifact area. Indeed, in average, it was −30% and −37% smaller for DW36 and DW20 when compared to DW90, respectively. As expected, the smallest area was obtained with SLT-2MLA (−80%) and SLT-4MLA (−56%).

TABLE IV shows that e_r was not significantly affected either by the flow rate or by the scan sequences. Moreover, e_r was reasonably low and always in the range [3.8%, 6%] with average values between 4.5% and 5.7%.

C. In-vivo images & clips

Fig. 6 and the accompanying clip 🎥 qualitatively compare the color Doppler images obtained with the different scan sequences during the filling phase of the LV. Moreover, panel

TABLE II
PATIENT'S SAFETY MEASUREMENTS

Modes	ΔT [°C]	MI	I_{spta} [mW/cm^2]	TIS	T_{ex} [min]
SLT-2MLA	8.6	0.48	146.4	1.08	120
SLT-4MLA	8.2	0.64	312.8	1.86	60
4MLT	8.8	0.35	78.5	1.15	120
DW20	8.0	0.56	134.6	1.68	60
DW36	8.4	0.40	56.4	1.54	60
DW90	7.9	0.26	13.3	0.62	>120

TABLE III
ESTIMATED SIZE OF ARTIFACTS AREA (A_A)
EXPRESSED IN PERCENTAGE WITH RESPECT TO DW90

Modes	Flow-rates [ml/min]				AVG
	300	360	420	480	
SLT-2MLA	−84	−73	−64	−98	−80
SLT-4MLA	−59	−56	−55	−54	−56
4MLT	−34	−20	−23	−20	−24
DW20	−38	−33	−41	−36	−37
DW36	−33	−28	−32	−28	−30
DW90	0	0	0	0	0

TABLE IV
AVERAGE RELATIVE ERROR (e_r) EXPRESSED IN PERCENTAGE

Modes	Flow-rates [ml/min]				AVG
	300	360	420	480	
SLT-2MLA	0.0	0.0	0.0	0.0	0.0
SLT-4MLA	4.4	4.8	5.2	5.1	4.9
4MLT	4.6	4.8	4.7	4.4	4.6
DW20	4.5	4.4	4.8	4.4	4.5
DW36	3.8	4.3	4.9	4.9	4.5
DW90	6.0	5.4	5.4	6.0	5.7

ST shows the temporal velocity profile for the different scan sequences that were extracted from the position highlighted by the white dot, i.e. at the inflow region in the left ventricle. In addition, since DW90 was not a scanned sequence, but consisted in the transmission of a single diverging wave, pulsed wave Doppler sonograms could be extracted at any position in the frame; an example of which is shown in panel PWD, where the sonogram was extracted for the white dot marker. The cyan line is the estimated flow velocity in CDI for the same point of interest. This estimate looks
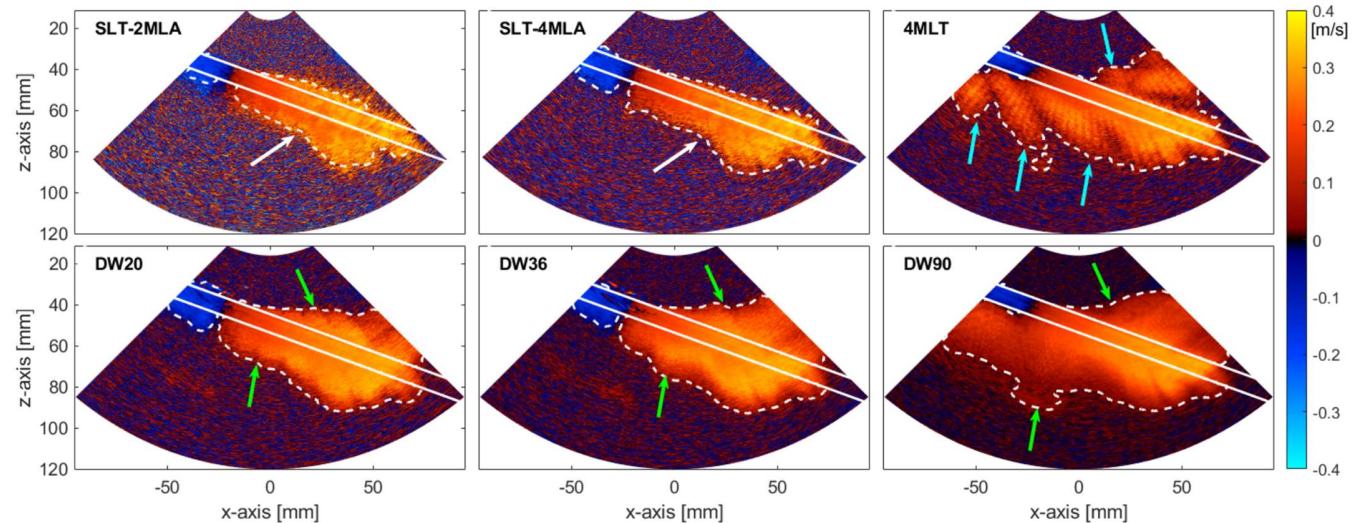

Fig. 5 Examples of CFI acquired on the flow phantom. The solid white parallel lines correspond to walls of the tube, while the dashed white lines surrond the artifact region estimated as described in section (II.D.3). The colorscale is in m/s. Arrows point to different artifact regions as detailed in section III.B.

underestimated during atrial systole, likely due to a residual of clutter on the negative speed, being higher than the cut-off speed (white dashed lines in panel PWD) of the polynomial regression filter used in CDI.

In the extracted CDI frames shown in Fig. 6, images look quite similar. The reddish clusters correspond to the blood flow, while the bluish clusters correspond to residual fast movements of the myocardium not filtered by the clutter-filter.

On the other hand, the accompanying clip shows the slow motion (1:8) of the CDI comparison. Specifically, it highlights that HFR images, compared to SLT sequences, allow a smoother transition between frames due to the higher temporal resolution. However, as shown in Fig. 5, HFR sequences generate artifacts affecting large parts of the image. As an example, during the opening of the mitral valve, happening from 0.4 to 0.8 s of the video clip time (i.e. from 0.05 to 0.10 s of the cardiac cycle), a red stripe, as wide as the image region, appears when using DW90. A similar effect can be observed for DW36 and DW20, but to a smaller extent, due to narrower opening angles of the diverging waves, whereas for 4-MLT the artifacts appear as 4 replicas of the main cluster. In SLT scan sequences, no artifacts can be observed during the mitral valve opening.

IV. DISCUSSION & CONCLUSION

In this paper, we have presented a study on high frame rate imaging for color flow echocardiography. Six different scan sequences, including SLT, MLT and DW, have been implemented on the Verasonics Vantage 256 system. A synthetic transmit beam technique was employed using an overlap of 50% between transmitted beams in order to reduce the amount of color Doppler artifacts due to parallel beamforming. Experimental data were acquired, both on a commercial Doppler flow simulator (with different flow velocity) and on healthy volunteers, and post-processed to reconstruct color Doppler images using the autocorrelation estimator. Images obtained with the different scan sequences were then compared both qualitatively and quantitatively.

In view of a possible clinical application, HFR sequences for CDI were compared considering the limitations due to patient safety, including protection against excessive surface temperatures and ultrasound radiation. The former, in our experience, is the main limitation in HFR imaging; hence, for a fair comparison, the acoustic output was equalized for all scan sequences. As shown in TABLE II, this equalization showed to be effective since the maximum temperature rise (ΔT) was similar for all sequences. Also, for the different scan sequences, ΔT was 8.35±0.45 °C, i.e. at least 1 °C below the
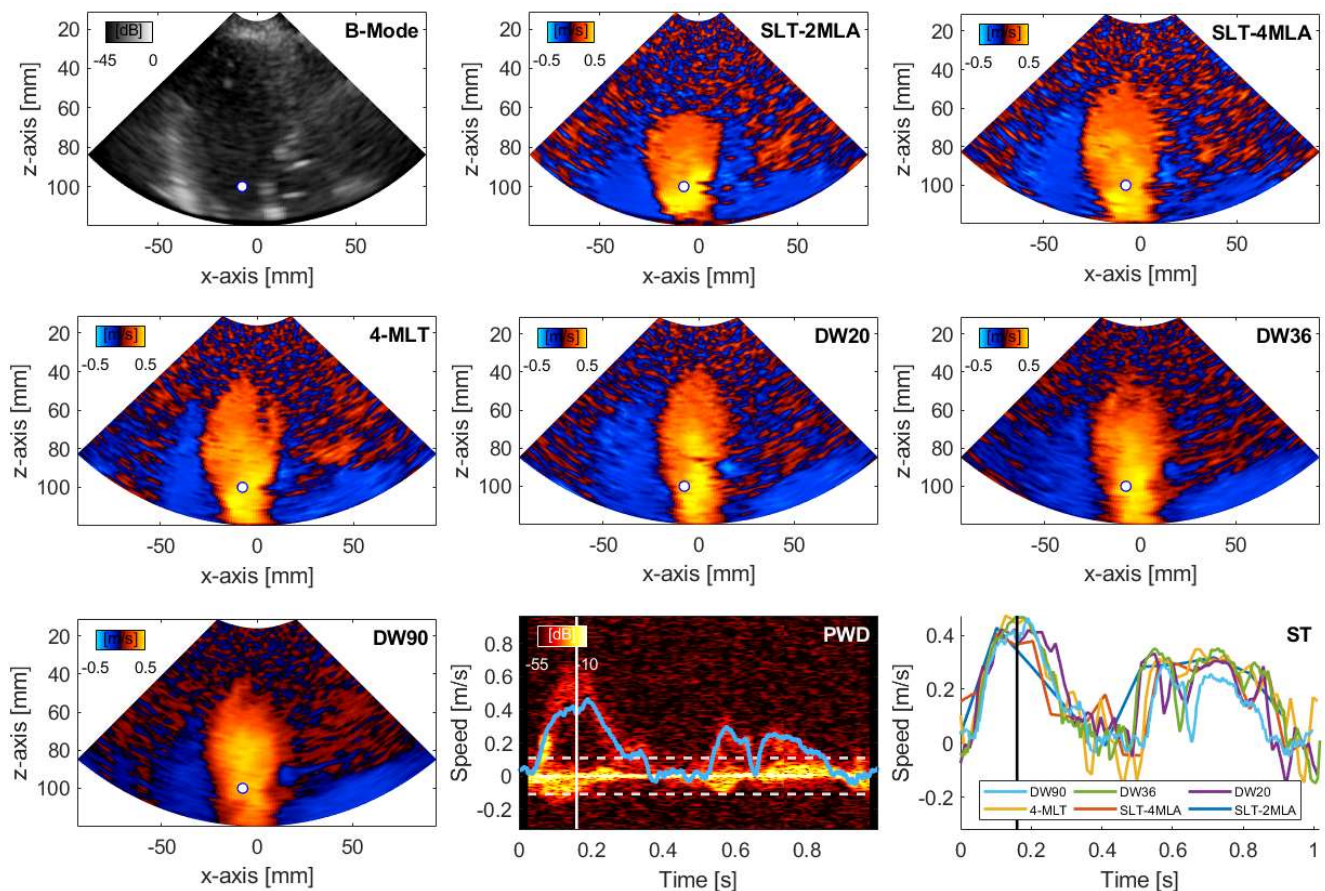

Fig. 6 Comparison of color Doppler images obtained for the different scan sequences during the systole of the left atrium. Panel B-mode shows the B-mode image obtained with SLT-2MLA. Panel ST shows the speed trend for the different scan sequences, which was extracted from the positions highlighted by the white dot markers. Panel PWD shows the pulsed wave Doppler sonogram obtained with the scan sequence DW90 and extracted from the position highlighted by the with dot marker in panel DW90; the dashed white lines highlight the cut-off frequency of the polynomial regression filter used in CDI; the cyan line is the estimated average flow speed.

maximum allowed limit (10 °C). The other parameters (MI, TI, I_{spta}) were well below the limits imposed by FDA. Unfortunately, as expected, such limitation plays against the achievable penetration depth of HFR sequences, as shown in Fig. 4. Indeed, for depths larger than 9 cm, the I_{ta} curves obtained with the different sequences (Fig. 4) drop at a similar rate. From that depth the average differences with respect to SLT-2MLA, when considering an attenuation of 0.5dB/cm/MHz, correspond to a reduction of the penetration depth by 1.3, 2.5, 2.8, 3.9, 5.1 cm, for SLT-4MLA, 4MLT, DW20, DW36, DW90, respectively. Such reduction could be significant in difficult-to-image patients, where the penetration depth in cardiac CDI is already an issue due to low signal-to-noise ratios as a result of the weak scattering properties of red-blood cells.

Color Doppler image quality was quantitatively assessed on phantom experiments in terms of size of the artifact area and relative error of the flow velocity estimates. It has been shown that, qualitatively, the artifacts generated with SLT sequences appear deeper than the tube and are mainly due to reverberations, multiple reflections and beam side lobes. On the other hand, for HFR sequences, artifacts are always generated as a combination of the effects of reflections/reverberations and the fact that the transmitted energy is spread along several directions simultaneously. The artifacts generated when using MLT are replicas of the main flow, with the number of replicas equal to the number of simultaneously transmitted beams; on the other hand, the artifacts of DWs generate a widespread band, the size of which widens with the opening angle of the transmitted DW. In order to have a quantitative evaluation of the size of the area affected by artifacts, the latter was automatically segmented showing that, compared to the worst case, i.e. DW90, SLT-2MLA had the narrowest artifacts area (−80% in average), whereas DW20 had the narrowest artifacts area among the HFR sequences (−37%). However, in general, HFR artifacts did not significantly affect the velocity estimates. Indeed, as shown in TABLE IV, e_r, i.e. the average relative error between velocity estimates with respect to SLT-2MLA, was reasonably low and always in the range [4.5%, 6%]. Actually, the differences in velocity error could be explained by the variability of Doppler estimates and not to a better or worse estimation of the flow velocity due to the imaging mode. Also, from a careful, qualitative comparison of the images shown in Fig. 5, the color Doppler frames obtained with focused scan sequences show some apparent spatial fluctuations of flow estimates inside the tube, which should be ascribed to the combination of the variability of Doppler estimates and short temporal smoothing. Indeed, those frames are obtained as the average over a time window of 1.0 s, hence, for scan sequences achieving higher frame rates, i.e. those obtained with defocused waves, more frames are averaged thus the final frames result smoothed.

Given the above premises, the method was tested on healthy volunteers showing the positive aspects and the limits of HFR scan sequences applied to CDI under patient safety constraints. As shown in Fig. 6, in the accompanying clip and

in agreement with TABLE IV, color Doppler images looked similar in the flow region. The main differences were flashing artifacts when fast moving, hyperechoic structures, e.g. valves, entered the region of interest. Nevertheless, in the presented examples, those artifacts did not impact on flow estimates as shown in panel ST of Fig. 6. Overall, the trends of the quantitative flow speed estimates obtained with the different scan sequences were similar, both in shape and amplitude, especially considering that they were taken on consecutive cardiac cycles that might be not identical. However, it is worth highlighting that residual clutter artifacts having an intensity comparable to that of blood signals, e.g. thus of moving valves of walls, may bias the estimation of blood flow velocity. Hence, scan sequences having smaller artifact areas (4MLT and DW20) should be preferred to those with a bigger artifact area (DW90), which may simultaneously jeopardize the velocity estimates on several point of the region of interest.

The main advantage of HFR CDI is the availability of flow information from a wide region of interest and with a high temporal resolution, both of which are limited in standard CDI. Specifically, since B-mode images and color Doppler images were obtained from the same scan sequences, the CDI frame rate (FR_{CDI}) was maximized, giving the values shown in TABLE V. Specifically, the frame rate achieved with SLT-2MLA, given the high number of imaging lines, is low (9.8 Hz) showing the limit of SLT imaging to provide a proper time resolution for quantitative use of color Doppler. On the other hand, HFR scan sequences achieved frame rates from 78 Hz up to 625 Hz. Moreover, we also showed that DW90, consisting in the transmission of a single, 90°-wide DW, allows computing pulsed wave Doppler, hence maximal and mean velocities, at any point of the region of interest, thereby overcoming the limitation of pulsed wave Doppler that is typically computed for a specific point or along a specific line.

Nevertheless, typically, duplex modes are employed to overlay color Doppler images on high quality B-mode images. Hence, a specific scan sequence for B-mode imaging is interleaved to that used for CDI thus reducing the achievable FR_{CDI}. TABLE V shows FR_{CDI} achievable in duplex mode, depending on the required frame rate in B-mode imaging. Specifically, the values reported in TABLE V considered a B-mode frame of 128 lines and a scan sequence based on SLT. As an example, if the required B-mode frame rate was 19.5 Hz (rightmost column of TABLE V), the FR_{CDI} would have been a half of that achieved without the duplex mode (leftmost column of TABLE V). Nevertheless, nowadays good B-mode imaging quality can be achieved also with HFR imaging techniques, thus reducing the number of transmission events required per B-mode frame and hence increasing the color Doppler frame rate also in duplex mode.

In conclusion, considering the limitations on penetration depth as well as the tradeoff between artifacts area and frame rate, the most promising HFR scan sequences seem to be 4MLT and DW20. However, when the penetration depth is not a main issue, e.g. in easy to image patients, DW36 and DW90 sequences might be applicable and may provide more information than 4MLT and DW20 sequences, owing to

higher temporal resolutions. Nevertheless, a follow-up study should be conducted to show which is the preferable sequence in a clinical scenario.

The clinical and diagnostic usefulness of HFR CDI is still an open point, as it is for other HFR imaging methodologies. Nevertheless, HFR CDI may pave the way to new applications that may find additional and relevant diagnostic information in a wider region of interest scanned at high temporal resolution. On our side, future perspectives of this study will include:

- A study to assess at which extent the same scan sequences and the same echo signals could be exploited for tissue Doppler imaging or speckle tracking, as already proposed for pulsed wave Doppler [39]. Hence, both blood and myocardial dynamics may be acquired in a single recording, rather than in two, thus improving the diagnostic information potentially available in blood-wall interactions, but also speeding up the clinical workflow thus improving cost-effectiveness.

- An extension of the study to assess the clinical applicability of 3D imaging techniques to CDI. Indeed, DWs have been shown to be effective in extracting the Doppler information either with the transmission of a single DW with a wide opening angle [40] or with multiple DWs with narrower opening angles [41].

Acknowledgment

References

[1] E. Wilkins *et al.*, "European Cardiovascular Disease Statistics 2017," *Eur. Heart Netw.*, Feb. 2017.

[2] E. J. Benjamin *et al.*, "Heart Disease and Stroke Statistics—2018 Update: A Report From the American Heart Association," *Circulation*, vol. 137, no. 2, pp. e67–e492, Jan. 2018.

[3] M. M. Redfield, S. J. Jacobsen, J. John C. Burnett, D. W. Mahoney, K. R. Bailey, and R. J. Rodeheffer, "Burden of Systolic and Diastolic Ventricular Dysfunction in the Community: Appreciating the Scope of the Heart Failure Epidemic," *JAMA*, vol. 289, no. 2, pp. 194–202, Jan. 2003.

[4] W. J. Bommer and L. Miller, "Real-time two-dimensional color-flow Doppler: Enhanced Doppler flow imaging in the diagnosis of cardiovascular disease," *Am. J. Cardiol.*, vol. 49, no. 4, p. 944, Mar. 1982.

[5] K. Miyatake *et al.*, "Clinical applications of a new type of real-time two-dimensional doppler flow imaging system," *Am. J. Cardiol.*, vol. 54, no. 7, pp. 857–868, Oct. 1984.

[6] T. L. Szabo, *Diagnostic Ultrasound Imaging: Inside Out*, 1st ed. Academic Press, 2004.

[7] F. Helmcke *et al.*, "Color Doppler assessment of mitral regurgitation with orthogonal planes.," *Circulation*, vol. 75, no. 1, pp. 175–183, Jan. 1987.

[8] J. Chambers, M. Monaghan, and G. Jackson, "Colour flow Doppler mapping in the assessment of prosthetic valve regurgitation.," *Br. Heart J.*, vol. 62, no. 1, pp. 1–8, Jul. 1989.

[9] F. Helmcke *et al.*, "Two-dimensional echocardiography and Doppler color flow mapping in the diagnosis and prognosis of ventricular septal rupture.," *Circulation*, vol. 81, no. 6, pp. 1775–1783, Jun. 1990.

[10] V. Mor-Avi *et al.*, "Current and Evolving Echocardiographic Techniques for the Quantitative Evaluation of Cardiac Mechanics: ASE/EAE Consensus Statement on Methodology and Indications Endorsed by the Japanese Society of Echocardiography," *Eur. J. Echocardiogr.*, vol. 12, no. 3, pp. 167–205, Mar. 2011.

[11] P. K. Woodard *et al.*, "ACR Appropriateness Criteria® Known or Suspected Congenital Heart Disease in the Adult," *J. Am. Coll. Radiol.*, vol. 14, no. 5, pp. S166–S176, May 2017.

[12] M. D. Cheitlin *et al.*, "ACC/AHA/ASE 2003 Guideline Update for the Clinical Application of Echocardiography: Summary Article," *Circulation*, vol. 108, no. 9, pp. 1146–1162, Sep. 2003.

[13] M. Tanter and M. Fink, "Ultrafast imaging in biomedical ultrasound," *IEEE Trans. Ultrason. Ferroelectr. Freq. Control*, vol. 61, no. 1, pp. 102–119, Jan. 2014.

[14] M. Cikes, L. Tong, G. R. Sutherland, and J. D'hooge, "Ultrafast Cardiac Ultrasound Imaging: Technical Principles, Applications, and Clinical Benefits," *JACC Cardiovasc. Imaging*, vol. 7, no. 8, pp. 812–823, Aug. 2014.

[15] L. Demi, "Practical Guide to Ultrasound Beam Forming: Beam Pattern and Image Reconstruction Analysis," *Appl. Sci.*, vol. 8, no. 9, p. 1544, Sep. 2018.

[16] B. Denarie *et al.*, "Coherent Plane Wave Compounding for Very High Frame Rate Ultrasonography of Rapidly Moving Targets," *IEEE Trans. Med. Imaging*, vol. 32, no. 7, pp. 1265–1276, Jul. 2013.

[17] B. F. Osmanski, D. Maresca, E. Messas, M. Tanter, and M. Pernot, "Transthoracic ultrafast Doppler imaging of human left ventricular hemodynamic function," *IEEE Trans. Ultrason. Ferroelectr. Freq. Control*, vol. 61, no. 8, pp. 1268–1275, Aug. 2014.

[18] H. Hasegawa and H. Kanai, "High-frame-rate echocardiography using diverging transmit beams and parallel receive beamforming," *J. Med. Ultrason.*, vol. 38, no. 3, pp. 129–140, May 2011.

[19] C. Papadacci, M. Pernot, M. Couade, M. Fink, and M. Tanter, "High-contrast ultrafast imaging of the heart," *IEEE Trans. Ultrason. Ferroelectr. Freq. Control*, vol. 61, no. 2, pp. 288–301, Feb. 2014.

[20] J. Poree, D. Posada, A. Hodzic, F. Tournoux, G. Cloutier, and D. Garcia, "High-Frame-Rate Echocardiography Using Coherent Compounding With Doppler-Based Motion-Compensation," *IEEE Trans. Med. Imaging*, vol. 35, no. 7, pp. 1647–1657, Jul. 2016.

[21] S. Fadnes, M. S. Wigen, S. A. Nyrnes, and L. Lovstakken, "In Vivo Intracardiac Vector Flow Imaging Using Phased Array Transducers for Pediatric Cardiology," *IEEE Trans. Ultrason. Ferroelectr. Freq. Control*, vol. 64, no. 9, pp. 1318–1326, Sep. 2017.

[22] R. Mallart and M. Fink, "Improved imaging rate through simultaneous transmission of several ultrasound beams," in *Proceedings of the SPIE*, 1992, vol. 1733, pp. 120–130.

[23] L. Tong, H. Gao, and J. D'hooge, "Multi-transmit beam forming for fast cardiac imaging-a simulation study," *IEEE Trans. Ultrason. Ferroelectr. Freq. Control*, vol. 60, no. 8, pp. 1719–1731, Aug. 2013.

[24] L. Tong, A. Ramalli, R. Jasaityte, P. Tortoli, and J. D'hooge, "Multi-Transmit Beam Forming for Fast Cardiac Imaging: Experimental Validation and In Vivo Application," *IEEE Trans. Med. Imaging*, vol. 33, no. 6, pp. 1205–1219, Jun. 2014.

[25] G. Matrone, A. Ramalli, A. S. Savoia, P. Tortoli, and G. Magenes, "High Frame-Rate, High Resolution Ultrasound Imaging With Multi-Line Transmission and Filtered-Delay Multiply And Sum Beamforming," *IEEE Trans. Med. Imaging*, vol. 36, no. 2, pp. 478–486, Feb. 2017.

[26] F. Prieur, B. Dénarié, A. Austeng, and H. Torp, "Correspondence - Multi-line transmission in medical imaging using the second-harmonic signal," *IEEE Trans. Ultrason. Ferroelectr. Freq. Control*, vol. 60, no. 12, pp. 2682–2692, Dec. 2013.

[27] International Electrotechnical Commission (IEC), "IEC 60601-2-37." Jun-2015.

[28] International Electrotechnical Commission (IEC), "EN 62359." Feb-2011.

[29] J. Grondin, V. Sayseng, and E. E. Konofagou, "Cardiac Strain Imaging With Coherent Compounding of Diverging Waves," *IEEE Trans. Ultrason. Ferroelectr. Freq. Control*, vol. 64, no. 8, pp. 1212–1222, Aug. 2017.

[30] T. Hergum, T. Bjastad, K. Kristoffersen, and H. Torp, "Parallel beamforming using synthetic transmit beams," *IEEE Trans. Ultrason.*

TABLE V
CDI FRAME RATE WITH AND WITHOUT DUPLEX MODE

Modes	FR_{CDI} [Hz]	FR_{CDI} in Duplex Mode [Hz]		
		B-mode @7.8 Hz	B-mode @13 Hz	B-mode @19.5 Hz
SLT-2MLA	9.8	7.8	6.5	4.9
SLT-4MLA	19.5	15.6	13.0	9.8
4MLT	78.1	62.5	52.1	39.1
DW20	78.1	62.5	52.1	39.1
DW36	156.2	125.0	104.2	78.1
DW90	625.0	500.0	417.0	312.5

Ferroelectr. Freq. Control, vol. 54, no. 2, pp. 271–280, Feb. 2007.

[31] T. Hergum, T. G. Bjastad, L. Løvstakken, K. Kristoffersen, and H. Torp, "Reducing color flow artifacts caused by parallel beamforming," *IEEE Trans. Ultrason. Ferroelectr. Freq. Control*, vol. 57, no. 4, pp. 830–838, Apr. 2010.

[32] H. Torp, "Clutter rejection filters in color flow imaging: a theoretical approach," *IEEE Trans. Ultrason. Ferroelectr. Freq. Control*, vol. 44, no. 2, pp. 417–424, Mar. 1997.

[33] S. Bjaerum, H. Torp, and K. Kristoffersen, "Clutter filter design for ultrasound color flow imaging," *IEEE Trans. Ultrason. Ferroelectr. Freq. Control*, vol. 49, no. 2, pp. 204–216, Feb. 2002.

[34] C. Kasai, K. Namekawa, A. Koyano, and R. Omoto, "Real-Time Two-Dimensional Blood Flow Imaging Using an Autocorrelation Technique," *IEEE Trans. Sonics Ultrason.*, vol. 32, no. 3, pp. 458–464, May 1985.

[35] J. A. Jensen, "FIELD: A Program for Simulating Ultrasound Systems," *Med. Biol. Eng. Comput.*, vol. 34, no. Supplement 1, Part 1, pp. 351–353, 1996.

[36] A. Ramalli *et al.*, "Real-Time High-Frame-Rate Cardiac B-Mode and Tissue Doppler Imaging Based on Multiline Transmission and Multiline Acquisition," *IEEE Trans. Ultrason. Ferroelectr. Freq. Control*, vol. 65, no. 11, pp. 2030–2041, Nov. 2018.

[37] A. Ramalli *et al.*, "Multi transmit beams for fast cardiac imaging towards clinical routine," in *2016 IEEE International Ultrasonics Symposium (IUS)*, 2016, pp. 1–4.

[38] G. ter Haar, "The new British Medical Ultrasound Society Guidelines for the safe use of diagnostic ultrasound equipment," *Ultrasound*, vol. 18, no. 2, pp. 50–51, May 2010.

[39] Y. Karabiyik, I. K. Ekroll, S. H. Eik-Nes, and L. Lovstakken, "Quantitative Doppler Analysis Using Conventional Color Flow Imaging Acquisitions," *IEEE Trans. Ultrason. Ferroelectr. Freq. Control*, vol. 65, no. 5, pp. 697–708, May 2018.

[40] C. Papadacci *et al.*, "4D simultaneous tissue and blood flow Doppler imaging: revisiting cardiac Doppler index with single heart beat 4D ultrafast echocardiography," *Phys. Med. Biol.*, vol. 64, no. 8, p. 085013, Apr. 2019.

[41] M. S. Wigen *et al.*, "4-D Intracardiac Ultrasound Vector Flow Imaging–Feasibility and Comparison to Phase-Contrast MRI," *IEEE Trans. Med. Imaging*, vol. 37, no. 12, pp. 2619–2629, Dec. 2018.